npj | 2D materials and applications

Article

Published in partnership with FCT NOVA with the support of E-MRS

https://doi.org/10.1038/s41699-025-00643-4

2D/2D heterojunction interfaces of 1T-MoS_2 and Ti_3C_2 MXene: designing high-performance catalyst for the hydrogen evolution reaction

Check for updates

Sana Akir[1] ✉, Bastian Schmiedecke[1], Debabrata Bagchi[2], Jan Plutnar[3], Prashanth W. Menezes[2,4], Yael Rodriguez-Ayllon[5,6], Yan Lu[5,6], Zdenek Sofer[3] & Michelle P. Browne[1] ✉

Designing efficient electrocatalysts for the hydrogen evolution reaction (HER) is crucial for advancing sustainable energy technologies. In this study, a 2D/2D heterostructure composed of 1T-phase molybdenum disulfide (1T-MoS_2) and titanium carbide MXene ($Ti_3C_2T_x$, denoted as Ti_3C_2) is synthesized using a one-step hydrothermal method. The hybrid catalyst exhibits improved HER kinetics, demonstrated by a low overpotential of 248 mV at 10 mA cm^{-2} and a Tafel slope of 55 mV dec^{-1}, indicating fast reaction kinetics and favorable charge transfer. The addition of tetramethylammonium ions (TMA^+) induces interlayer expansion, increasing the 1T phase content to 89%. Incorporating only 1% Ti_3C_2 MXene suppresses oxidation and enhances stability. The composite demonstrates a large electrochemical surface area, high turnover frequency (TOF), and retains over 90% of its catalytic activity after extended electrolysis. This scalable approach offers a promising route to developing stable, efficient 2D electrocatalysts for hydrogen production.

The global transition to sustainable energy solutions has driven an urgent need for efficient, carbon-free energy sources. Hydrogen, as a clean and renewable energy carrier, has gained significant attention due to its high gravimetric energy content and environmentally benign byproducts[1,2]. Among various hydrogen production methods, electrochemical water splitting is considered one of the most promising and environmentally friendly approaches. However, the practical deployment of this approach relies on the availability of highly active and durable electrocatalysts for the hydrogen evolution reaction (HER). Platinum (Pt)-based catalysts have long been the benchmark for HER due to their outstanding catalytic activity and stability. However, the scarcity and high cost of Pt have driven the search for alternative materials that are cost-effective, scalable, and capable of delivering comparable performance[3]. Transition metal dichalcogenides (TMDs) have emerged as promising candidates for HER due to their distinctive electronic features and adjustable catalytic behavior[4–8]. Among them, molybdenum disulfide (MoS_2) is particularly attractive due to its abundance, layered structure, favorable hydrogen adsorption energy (ΔG_H^* ≈ 0.08 eV at edge sites)[9] and various structural engineering possibilities[6]. The properties of MoS_2 are significantly influenced by its polymorphic phases, especially the hexagonal 2H phase and the octahedral 1T phase. The semiconducting 2H phase has an inherent low electrical conductivity, which restricts the performance of MoS_2-based electrocatalysts[10]. In contrast, the metallic 1T phase exhibits improved conductivity and catalytically active basal planes, making it exceptionally suitable for HER applications. To enhance the conductivity of 2H-MoS_2, significant efforts have been made to induce a phase transition from the 2H phase to the metallic 1T phase. This can be achieved through various techniques, including ion intercalation, doping, and strain engineering[5,6]. Among these methods, ion intercalation is particularly appealing due to its practicality and ease of integration into hydrothermal or solvothermal synthesis, thereby eliminating the need for additional post-treatment steps[11]. It was reported that the intercalation of foreign ions into the layers of MoS_2 reduces the van der Waals forces

[1]Helmholtz Young Investigator Group Electrocatalysis: Synthesis to Devices, Helmholtz-Zentrum Berlin für Materialien und Energie, Berlin, Germany. [2]Department of Materials Chemistry for Catalysis, Helmholtz-Zentrum Berlin für Materialien und Energie, Albert-Einstein-Str. 15, Berlin, Germany. [3]Department of Inorganic Chemistry, University of Chemistry and Technology Prague, Prague 6, Czech Republic. [4]Department of Chemistry: Metalorganics and Inorganic Materials, Technische Universität Berlin, Berlin, Germany. [5]Institute of Electrochemical Energy Storage, Helmholtz-Zentrum Berlin für Materialien und Energie, Berlin, Germany. [6]Institute for Technical and Environmental Chemistry, Friedrich-Schiller-Universität Jena and Helmholtz Institute for Polymers in Energy Applications (HIPOLE Jena), Jena, Germany. ✉e-mail: sana.akir_ep_benabdelhafidh@helmholtz-berlin.de; Michelle.browne@helmholtz-berlin.de

between adjacent layers by increasing the interlayer spacing, thus promoting the transformation to the 1T phase[12]. Various cations, neutral molecules, and solvents, including Li^+, Na^+, Ca^{2+}, Ni^{2+}, Co^{2+}, NH_4^+, TMA^+, Zn_{2+}, NH_3, and DMF, have been reported to facilitate this phase transition[13]. Among them, tetramethylammonium (TMA^+) ions are particularly effective due to their bulky organic structure, which expands the interlayer distance while remaining compatible with aqueous environments. TMA^+ intercalation has been shown to enlarge the spacing between layers, thereby stabilizing the metastable 1T phase. In a notable study, Jin et al. demonstrated that in situ TMA^+ cation intercalation produced MoS_2 nanosheets containing ~81% 1T phase and abundant sulfur vacancies, as confirmed by AC-HAADF-STEM, XPS, and XAFS analyses[14]. Additionally, it was reported that inserting TMA^+ into the interlayers of MoS_2 nanosheets expands the interlayer spacing and simultaneously causes distortion of the atomic arrangement. This process contributes to the formation of numerous 1T phases and grain boundary defects, which accordingly increase the active sites for hydrogen production[10].

MXenes, another family of 2D materials, have attracted significant interest due to their exceptional intrinsic properties[15]. With the general formula $M_{n+1}X_nT_x$, where M is an early transition metal, X represents carbon and/or nitrogen, and T_x refers to surface functional groups. MXenes are produced by selectively etching the A-element from MAX phases, where A is typically an element from groups IIIA or IVA[16]. MXenes exhibit highly hydrophilic surfaces (functionalized with -O, -OH, and/or -F groups), remarkable metallic conductivity (e.g., $Ti_3C_2 \sim 9880\ S\ cm^{-1}$), and a large interlayer distance[17,18]. These characteristics make MXenes ideal conductive matrices for anchoring and nucleating other active materials[17,19,20]. However, due to the high proportion of exposed metal atoms on the surface, MXenes are usually thermodynamically metastable with high surface energy, and suffer from poor oxygen resistance in air or oxygen-dissolved solutions even at ambient conditions[5,18,21]. This oxidation leads to structural degradation, compromising their electrical and electrochemical properties. Therefore, creating effective strategies to reduce oxidation is essential for the practical use of MXenes. Furthermore, oxidation is difficult to prevent using common nanomaterial manufacturing methods, such as hydrothermal synthesis, solvothermal synthesis, calcination, and refluxing. This limitation hinders both the full exploitation of MXenes and a deeper understanding of their chemical nature[22]. To overcome this limitation, encapsulating the surface of MXenes with another material has been explored as a promising solution. Recent studies have focused on fabricating 2D/2D heterostructures that combine MXenes with MoS_2. These hybrid structures utilize the synergistic effects of both materials to prevent layer restacking and improve catalytic activity[5]. Recently, 2H-MoS_2 has been combined with various MXenes through in-situ sulfidation[23] and microwave-assisted growth techniques[24]. Although these methods have demonstrated enhanced catalytic activity and durability for HER, they often require complex, multi-step processes that need sophisticated equipment, making them expensive and time-consuming. Furthermore, the inherently low electrical conductivity of 2H-MoS_2 remains a significant barrier to achieving optimal catalytic performance in these composites. Hydrothermal synthesis has also been investigated to produce 2H-MoS_2/MXene composites[25], but the low electrical conductivity of the 2H-phase MoS_2 remains a significant obstacle, hindering overall catalytic efficiency.

In this work, we present a facile one-step hydrothermal method for synthesizing a 1T-MoS_2/Ti_3C_2 MXene heterostructure. For simplicity, $Ti_3C_2T_x$ is hereafter denoted as Ti_3C_2 throughout the manuscript. Unlike previously reported approaches, which often require multi-step procedures, carbon coating, or sophisticated equipment, our method enables the direct formation of a stable 2D/2D composite without post-treatment or protective barriers. In this synthesis, MoS_2 nanosheets are uniformly intercalated between Ti_3C_2 layers, forming a tightly integrated heterostructure. A key innovation of our strategy is the use of tetramethylammonium hydroxide (TMAOH), which plays a dual role: it promotes the phase transition of MoS_2 from the 2H to the more conductive 1T phase and simultaneously enables the formation of a stable, oxidation-resistant 2D/2D composite without the need for complex equipment or additional post-treatment. This method not only simplifies the fabrication process but also significantly enhances the electrochemical performance of the resulting composite. The 1T-MoS_2/Ti_3C_2 heterostructure exhibits a favorable Tafel slope of 55 mV dec^{-1} and an overpotential of 248 mV at 10 mA cm^{-2}, despite containing only 1% Ti_3C_2 MXene. These values are competitive with or superior to previously reported Ti_3C_2/MoS_2-based catalysts, confirming the synergistic effect of the 2D/2D interface, which offers abundant active sites and efficient charge transfer pathways. Additionally, the composite demonstrates exceptional durability and operational stability over 15 h in acidic electrolyte, highlighting its potential for practical hydrogen evolution applications. Overall, this work provides a cost-effective, scalable, and oxidation-resistant strategy for integrating MXenes with 1T-phase MoS_2, advancing the development of efficient non-precious metal HER electrocatalysts.

Results

Characterization of electrocatalysts

The crystallographic structure and phase composition of the synthesized catalyst were investigated using X-ray diffraction (XRD) and Raman spectroscopy. Figure S1a displays the XRD profiles of both Ti_3C_2 MXene and its precursor Ti_3AlC_2 MAX phase. The Ti_3C_2 pattern shows distinct reflections at 6.15°, 18.17°, and 27.7°, which correspond to the (002), (004), and (006) planes, respectively, indicating layered MXene formation[5]. In contrast, the peak around 38.7°, typically associated with aluminum (Al) in Ti_3AlC_2, disappears after etching, confirming successful removal of the Al layers and formation of Ti_3C_2[26]. Using Bragg's law, the calculated interlayer spacing for Ti_3C_2 is ~1.42 nm, consistent with literature values[27,28]. The XRD spectrum of 2H-MoS_2 exhibits sharp peaks at 14.1°, 33.4°, and 58.8°, corresponding to the (002), (100), and (110) reflections of its hexagonal phase ($P6_3/mmc$, JCPDS 37-1492)[29,30]. A comparison with the 1T-MoS_2 pattern shows a shift of the (002) peak from ~14° to around 9°, indicating an increase in interlayer distance. Moreover, the disappearance of the peak at ~14° implies the formation of a few-layered MoS_2. The broadening and shifting of the (100) and (110) peaks to lower angles, along with the emergence of a (004) reflection at ~18.2°, suggest distortion and phase transition to the metallic 1T-MoS_2 phase[11]. These observations confirm the crucial role of tetramethylammonium hydroxide (TMAOH) in promoting 1 T phase formation. The intercalation of TMA^+ ions between the MoS_2 layers expands the interlayer spacing and induces distortions in the atomic arrangement. This process promotes the formation of the 1T phase and generates numerous grain boundary defects, which enhance the density of active sites for hydrogen production[10]. This interpretation is further supported by the increase in (002) d-spacing from 0.63 nm (2H phase) to 0.97 nm (1T phase). To directly assess the intercalation of TMA^+ and its influence on phase transformation, we performed thermogravimetric analysis (TGA) on both 2H-MoS_2 and 1T-MoS_2 after TMAOH treatment. As shown in Fig. S1c, the 2H-MoS_2 sample exhibited a total mass loss of ~8 wt% up to 800 °C, primarily due to desorption of surface-bound water and minor structural changes. In contrast, the TMAOH-intercalated 1T-MoS_2 exhibited a significantly larger mass loss of around 22.5 wt%, with a distinct weight loss event observed between 200 °C and 400 °C. This thermal behavior indicates the presence and subsequent decomposition of intercalated organic species (TMA^*), providing strong evidence for successful intercalation and structural modification toward the 1T phase. This interpretation is consistent with previous reports, which show that the decomposition of TMA^* occurs between 200 °C and 400 °C, contributing to a similar weight loss in the TMAOH-intercalated MoS_2 sample[31]. It should be noted that the hydrothermal synthesis temperature (200 °C) lies at the lower edge of the TMA^* decomposition range (200–400 °C) identified by TGA, ensuring that the intercalated cations remain stable during synthesis and effectively promote the 1T phase formation. Therefore, no thermal reversion to the 2H phase is expected under the employed conditions. Furthermore, in the Ti_3C_2/1T-MoS_2 composites (TM-2 through TM-10), XRD peaks indicative of both MXene and 1T-MoS_2 are present. The Ti_3C_2 peak is absent in TM-1, likely due to its low loading. In all MoS_2/Ti_3C_2 composites (TM-2 to TM-10), the (002) diffraction peak of Ti_3C_2 shifts slightly to 7.15° after hydrothermal synthesis at 200 °C. This shift indicates a small decrease in

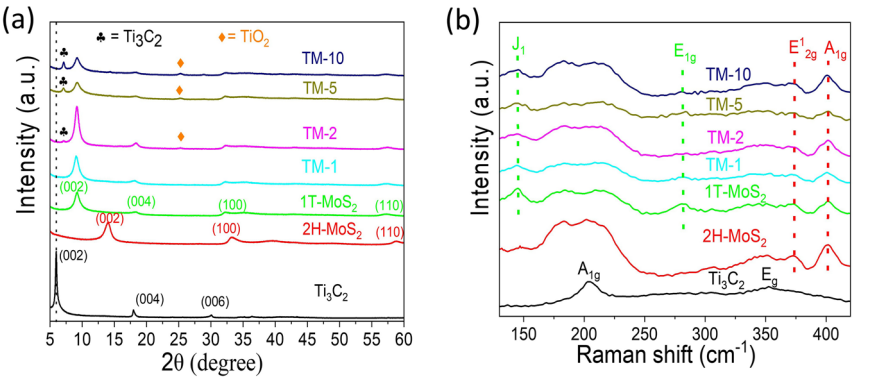


Fig. 1 | Structural characterization. a XRD patterns of Ti_3C_2 MXene, 1 T-MoS_2, 2H-MoS_2, and (TM-1, TM-2, TM-5 and TM-10) composites, **b** RAMAN of $Ti_3C_2T_x$ MXene, 2H-MoS_2, 1T-MoS_2, and (TM-1, TM-2, TM-5 and TM-10) composites.

the interlayer spacing of $Ti_3C_2T_x$, which can be attributed to the partial removal or rearrangement of interlayer water molecules and surface terminal groups (-OH, -O, -F) during the hydrothermal treatment. This observation is consistent with previously reported MXene-based heterostructures prepared under similar hydrothermal conditions, which also exhibited a minor shift in the (002) peak[28,32]. Notably, the (002) diffraction peak of Ti_3C_2 in these composites remains at a low angle (~7.15°), indicating that the MXene structure remains delaminated and highly expanded even after hydrothermal processing at 200 °C. This suggests that the interlayer spacing is still significantly increased, likely due to the retention of intercalated TMA^+ ions and 1T-MoS_2 nanosheets between the Ti_3C_2 layers, consistent with previous reports[33]. Additionally, a minor peak at 25.35° in samples with >1% MXene (Fig. S1b) suggests trace formation of TiO_2, likely due to surface oxidation of Ti under synthesis conditions. This peak is notably absent in TM-1, supporting the conclusion that low MXene content helps preserve structural integrity and promotes efficient charge transport. Another noteworthy feature in TM-10 is the reappearance of a (002) peak at $2\theta \approx 14.4°$, indicating the stacking of MoS_2 layers (Fig. S1b). This may imply partial transformation back to the 2H phase under high MXene loading, which could impact electronic properties. Raman spectroscopy provided further insights into the materials' microstructure (Fig. S1d and Fig. 1b). The Ti_3C_2 MXene sample exhibited characteristic peaks at 126, 209, 359, and 723 cm^{-1}, in agreement with typical vibrations of delaminated MXenes, corresponding to A_{1g} (Ti, O, C), E_g (O), and A_{1g} (C) modes, respectively[26,34]. Figure 1b shows Raman spectra for 2H-MoS_2, 1T-MoS_2, and composites. Considering 2H-MoS_2, the characteristic peaks appearing at 373 and 401 cm^{-1} are assigned to the A_{1g} and E^1_{2g} bonds of the 2H phase, respectively[24]. The intensity of the out-of-plane A_{1g} mode surpasses that of the in-plane E^1_{2g} mode, suggesting an edge-enriched MoS_2 structure[24]. Upon TMA^+ treatment, the MoS_2 bands decreased in intensity, and a new band at 145 cm^{-1} (J_1 mode) emerged, indicating successful formation of the 1T phase. A further signal at ~283 cm^{-1} (E_{1g}) confirmed the presence of Mo atoms in octahedral coordination, characteristic of 1T-MoS_2[30]. The composite spectra (TM-1 to TM-10) showed similar vibrational features. Notably, TM-1 exhibited the weakest signals related to 2H-MoS_2, suggesting a more complete phase conversion. In contrast, TM-10 showed increased 2H-character, corroborating the XRD findings. Additionally, the peak intensity of Ti_3C_2, observed at ~205 cm^{-1} across all composites, appears notably flat. This reduced intensity is attributed to the surface of the Ti_3C_2 MXene being covered by a layer of 1T-MoS_2, coupled with the intrinsically weak signal characteristics of Ti_3C_2. Consequently, the laser cannot penetrate the MoS_2 layer effectively, resulting in limited information about the underlying Ti_3C_2 MXene[18].

The surface morphology of the synthesized catalysts was examined using scanning electron microscopy (SEM). As illustrated in Fig. S1e, Ti_3C_2 MXene displays exfoliated, layered nanosheets with a distinct and organized structure. The inset further reveals its micrometer-scale dimensions, which offer a suitable platform for the uniform deposition of MoS_2 layers. SEM imaging of 2H-MoS_2 (Fig. 2a) presents a flower-like morphology with a tendency for sheet aggregation. In contrast, the 1T-MoS_2 sample exhibits a more flake-like texture, indicating structural variation between the two phases (Fig. 2a). In the composite samples (Fig. 2c–e), MoS_2 sheets are observed to grow both within the interlayer spaces and across the surface of the Ti_3C_2 MXene. This layered Ti_3C_2/1T-MoS_2 configuration mitigates nanosheet restacking and concurrently shields the oxidation-sensitive Ti_3C_2 structure[6], a finding consistent with the XRD results. Interestingly, even though deionized water was used during hydrothermal treatment, the TM-1 composite (with 1% MXene) showed negligible signs of oxidation, while slight oxidation was detected in samples with higher MXene content. This suggests that tetramethylammonium (TMA^+) ions play a stabilizing role during synthesis, encouraging 1T-MoS_2 phase formation and reducing oxidative degradation of the MXene, as previously observed in related studies[6,35]. Closer inspection (inset of Fig. 2c) reveals that the MoS_2 nanosheets closely overlay the Ti_3C_2 layers, forming a compact heterostructure. This architecture promotes greater exposure of catalytic sites and enhances diffusion pathways for hydrogen evolution reaction (HER) processes[24].

To confirm the structural integrity of Ti_3C_2 in the TM-1 composite and assess the potential formation of TiO_2 during hydrothermal treatment, a combination of high-resolution transmission electron microscopy (HRTEM), scanning transmission electron microscopy with energy-dispersive X-ray spectroscopy (STEM-EDS) was employed. TEM analysis of the Ti_3C_2 MXene (Fig. S2a) displayed its characteristic few-layered, sheet-like morphology, confirming its two-dimensional nature. The HRTEM image (Fig. S2b) showed distinct lattice fringes with a spacing of around 0.52 nm, corresponding to the (004) crystallographic planes, in agreement with interlayer distances measured via XRD. Additionally, selected area electron diffraction (SAED) patterns (inset of Fig. S2b) indicated a hexagonal symmetry typical of Ti_3C_2. For 2H-MoS_2, the TEM images (Fig. S2c) revealed aggregated nanosheets, while the observed d-spacing of ~0.62 nm aligned with the (002) plane, confirming its layered structure. A structural transition to the 1T phase was evidenced by increased interlayer spacing (~0.92 nm) and lattice distortion seen in HRTEM (Fig. S2f), characteristics associated with the metallic 1T form of MoS_2. Notably, the 1T-MoS_2 exhibited a thin, few-layered architecture, an advantageous feature that promotes efficient ion transport and electron mobility during electrocatalytic processes. In the case of the TM-1 composite, both TEM and HRTEM (Fig. 3a, b) revealed a homogeneous hybrid architecture, where 1T-MoS_2 nanosheets were well-dispersed across the MXene substrate, forming a cohesive 2D network. HRTEM images (Fig. 3b) revealed well-defined lattice fringes corresponding to the (002) plane of Ti_3C_2 (~1.1 nm) alongside the (002) plane of 1T-MoS_2 (~0.9 nm), confirming that the MXene structure remains intact after synthesis. Notably, no TiO_2 nanoparticles were observed on the surface of the MXene, in contrast to previous reports where hydrothermal treatment led to the formation of TiO_2 nanocrystals[6]. STEM-EDS elemental mapping (Fig. 3c) further confirmed the homogeneous distribution of Ti, C, Mo, S, and O, with no localized oxygen enrichment indicative of oxide formation. The relatively intense and widely distributed C signal observed in the EDX mapping is partly attributed to the carbon-coated TEM support grid, which contributes a uniform background carbon

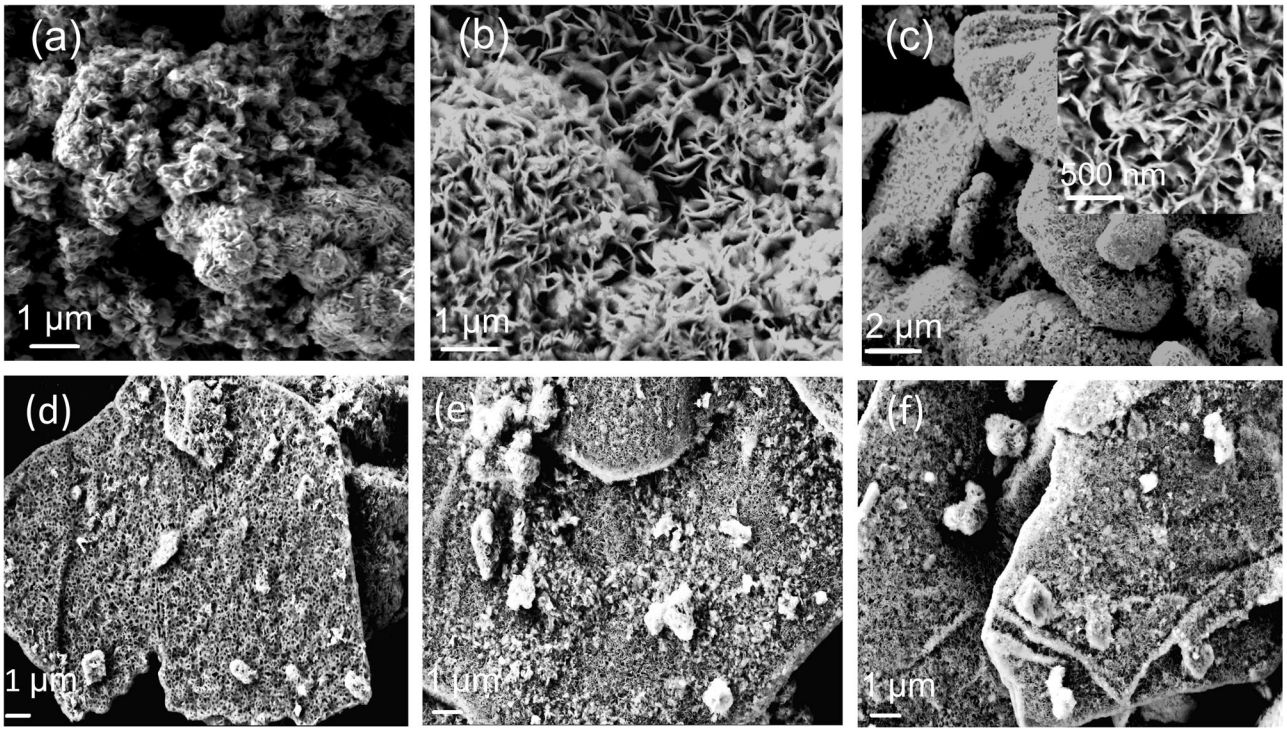


Fig. 2 | Surface morphology of MoS_2 phases and Ti_3C_2/1T-MoS_2 composites. SEM of **a** 2H-MoS_2, **b** 1 T-MoS_2, **c** TM-1, **d** TM-2, **e** TM-5, **f** TM-10.

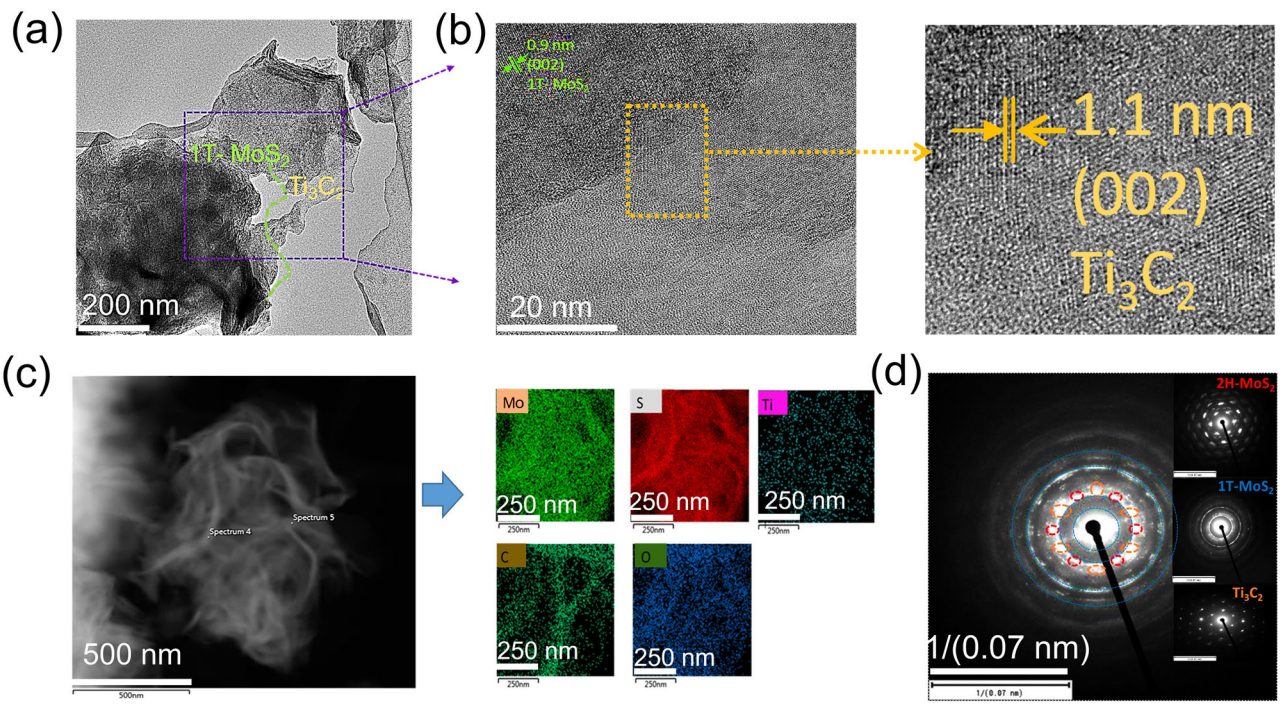


Fig. 3 | TEM characterization. a TEM of TM-1, **b** HRTEM of TM-1, **c** STEM-EDX mapping images of Mo, S, C, O, and Ti of TM-1 heterostructure, and **d** SAED pattern of TM-1 (inset: SAED patterns of 2H, 1T-MoS_2, and Ti_3C_2).

layer. The O/Ti atomic ratio, determined from EDS spectra of Ti_3C_2 before and after hydrothermal treatment at 200 °C, was ~0.53, closely matching that of freshly prepared, minimally oxidized Ti_3C_2 (0.46, Fig. S2g). In contrast, aged or hydrothermally oxidized MXenes typically exhibit significantly higher O/Ti ratios, reflecting extensive TiO_2 formation. Additionally, neither the XRD patterns nor the Raman spectra of TM-1 displayed any signatures of crystalline TiO_2, further confirming the chemical stability of Ti_3C_2 under the applied hydrothermal conditions. This exceptional structural preservation is attributed to the presence of TMAOH, used both during the initial delamination of MXene and in small quantities during the in-situ synthesis of the 1T-MoS_2/Ti_3C_2 composite. Beyond facilitating delamination through TMA^+ intercalation, TMAOH acts as a pH buffer and surface passivating agent. Literature reports have shown that ammonium-based hydroxides, such as NH_4OH and TMAOH, stabilize Ti_3C_2 in aqueous media by maintaining the dispersion pH around 6–7, a range where MXenes remain colloidally stable for extended periods without

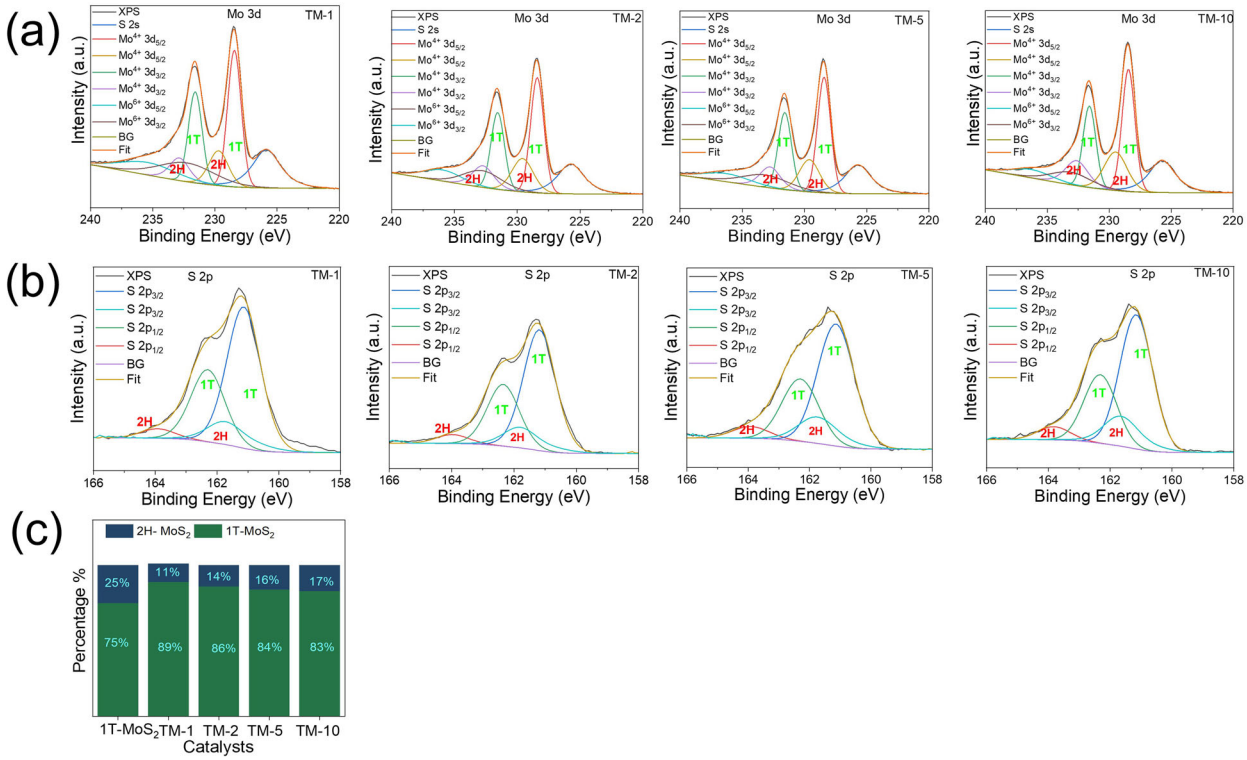


Fig. 4 | X-ray photoelectron spectroscopy analysis. Deconvoluted XPS spectra of **a** Mo 3d and **b** S 2p for TM-1, TM-2, TM-5, and TM-10 composites, and **c** Relative fraction of 1 T and 2H phase in 1T-MoS_2 and composites.

significant aggregation or oxidation. For instance, NH_4OH-treated Ti_3C_2 has been reported to remain stable for over 40 days at pH ~6, whereas oxidation and sedimentation accelerate under acidic conditions or when pH exceeds 12 due to flocculation and hydrolysis[36,37]. The mildly basic environment provided by TMAOH during our synthesis likely suppresses hydrolytic degradation and preserves interlayer TMA^+ cations, both of which contribute to protecting Ti sites from oxidation.

SAED analysis of the TM-1 composite (Fig. 3d) reveals several well-defined diffraction rings, highlighted in blue. These rings are characteristic of polycrystalline 1T-MoS_2 and indicate the presence of numerous randomly oriented nanocrystalline domains, consistent with previous reports on chemically stabilized 1T-MoS_2[37,38]. In addition to the 1T-MoS_2 pattern, distinct diffraction spots corresponding to Ti_3C_2 MXene and 2H-MoS_2 are also observed, confirming the coexistence of multiple structural phases within the composite.

X-ray photoelectron spectroscopy (XPS) analysis was conducted to investigate the elemental composition and surface chemical states of Ti_3C_2 and its composites. The full survey scan for pristine Ti_3C_2, as shown in Fig. S3a, displays distinct signals corresponding to C 1 s, Ti 2p, O 1 s, and F 1 s. Notably, no aluminum peaks were detected, confirming the complete etching of Al layers from the precursor MAX phase. The presence of oxygen- and fluorine-containing groups is consistent with HF treatment, which introduces functional surface terminations. The high-resolution Ti 2p spectrum (Fig. S3b) reveals four prominent peaks: those at around 455.8 eV and 461.8 eV are assigned to Ti $2p_{3/2}$ and Ti $2p_{1/2}$ in Ti-C bonds, respectively. Peaks at higher binding energies (~459.3 eV and ~465.1 eV) indicate Ti-O bonding, suggesting the formation of TiO_2 species, likely due to surface oxidation. The C 1 s spectrum (Fig. S3c) includes a main peak at 282.4 eV related to Ti-C bonding, confirming Ti_3C_2 formation[39]. Additional peaks at 285.1 eV, 286.7 eV, and 289.4 eV are attributed to adventitious carbon, C-O, and C=O functionalities, respectively, likely arising from atmospheric exposure and residual surface groups[40,41]. The O 1 s spectrum (Fig. S3d) displays peaks at 529.5 eV and 531.3 eV, which correspond to hydroxylated and oxidized Ti sites (C-Ti-OH and C-Ti-O), further indicating the presence of -OH and -O terminations on the MXene surface due to selective etching[30]. Also, the complete survey XPS spectra of the composites are shown in Fig. S3a. Only signals corresponding to S 2p, Mo 3d, C 1s, and O 1s are detected, while no distinct Ti 2p signals are observed. This absence of Ti peaks suggests that the MoS_2 layer fully covers the Ti_3C_2 MXene surface, effectively shielding it from XPS detection. This behavior is consistent with previous reports in the literature[42,43]. The Mo 3d spectrum of all prepared composites (Fig. 4a) displays prominent peaks at 228.4 eV and 231.5 eV corresponding to the Mo^{4+} $3d_{5/2}$ and Mo^{4+} $3d_{3/2}$ characteristic peaks of 1T-MoS_2, respectively. Additional weaker signals located at 232.6 and 229.7 eV correspond to the characteristic $3d_{5/2}$ and $3d_{3/2}$ of Mo^{4+} species from the non-metallic 2H phase[18], both of which were also detected in the 2H-MoS_2 sample (Fig. S3e). Furthermore, the peak at 235.6 eV illustrates Mo^{6+}, suggesting the partial oxidation of MoS_2[30]. A low-intensity peak at 225.6 eV corresponds to the S 2s. Upon deconvolution of the S 2p spectrum (Fig. 4b), two principal peaks appear at 161.1 eV and 162.3 eV, assigned to S $2p_{3/2}$ and S $2p_{1/2}$ of the 1T-MoS_2 phase, respectively[5]. Minor peaks at 161.7 eV and 163.8 eV reflect the corresponding signals from the 2H phase. These assignments were further validated by comparison with the XPS spectra of individual 1T- and 2H-MoS_2 reference samples (Fig. S3g and S3h), which exhibit consistent peak positions and spectral profiles. Additionally, the full-width at half-maximum (FWHM) values of the deconvoluted peaks are summarized in Table S1a, further supporting the reliability of the fitting and the accuracy of the 1T/2H peak assignments. The relative 1T phase content was quantified by integrating the areas of the deconvoluted S $2p_{3/2}$ and S $2p_{1/2}$ peaks assigned to 1T- and 2H-MoS_2, and calculating the ratio of the 1T signal area to the total S 2p area (Table S1b). As illustrated in Fig. 4c, all composites (TM-1, TM-2, TM-5, and TM-10) exhibit a larger proportion of the 1T phase compared with pristine 1T-MoS_2. This enhancement arises from interfacial charge transfer and structural distortion at the Ti_3C_2/MoS_2 junction. The metallic Ti_3C_2 layers inject electrons into MoS_2, stabilizing the metallic 1T configuration, while interfacial strain and TMA^+ intercalation further promote and preserve this phase during hydrothermal synthesis. It is worth noting that a high proportion of 1T-MoS_2 is advantageous for HER

performance due to its enhanced electronic conductivity and higher density of catalytically active sites.

Electrocatalytic performance for HER

The HER performance of the synthesized materials was assessed using a conventional three-electrode system in 0.5 M H_2SO_4, with iR-compensation applied throughout. A commercial Pt/C catalyst (20 wt%) and a bare glassy carbon (GC) electrode served as performance references. As depicted in Fig. 5a, the GC electrode showed negligible catalytic activity, confirming that the measured performance originates from the tested materials. Predictably, Pt/C delivered outstanding HER efficiency, requiring just 34 mV to reach a current density of 10 mA cm^{-2} (Fig. 5b), reaffirming its status as a benchmark catalyst. In contrast, pure Ti_3C_2 MXene displayed relatively poor HER activity, with an overpotential of 770 mV at 10 mA cm^{-2}. This suggests that while it is not intrinsically active, Ti_3C_2 serves as a conductive substrate that facilitates electron transport in hybrid systems. Meanwhile, 1T-MoS_2 significantly outperformed its 2H counterpart, achieving an overpotential of 278 mV compared to 369 mV, respectively, an improvement attributed to the stabilization of the 1T phase via TMA^+ ion intercalation. To further investigate HER enhancement, 1T-MoS_2 was combined with varying amounts of Ti_3C_2 (1, 2, 5, and 10 wt%) to form hybrid composites denoted as TM-1, TM-2, TM-5, and TM-10. Among these, TM-1 exhibited the most promising activity, achieving an overpotential of ~248 mV at 10 mA cm^{-2}. However, higher MXene loadings led to decreased performance; for example, TM-10 required 309 mV at the same current, implying that excessive Ti_3C_2 may obscure the active MoS_2 surface, thereby hindering catalytic efficiency. For comparison, a physically blended sample (PM-1) was also prepared by mixing pre-synthesized 1T-MoS_2 with 1 wt% Ti_3C_2 in a 1:1 water-isopropanol solution, followed by ultrasonication (4 h), filtration, and vacuum drying at 70 °C. As shown in Fig. 5a, PM-1 required a much higher overpotential (334 mV) to achieve 10 mA cm^{-2}, substantially underperforming relative to TM-1 (~248 mV). This result emphasizes the significance of the synthesis strategy; unlike the hydrothermally grown TM-1, the physical mixture demonstrated weak interfacial contact between components, which restricted charge transfer and overall HER activity[44].

To gain further insights into the reaction mechanism and kinetics of HER, Tafel slope analysis was conducted. A lower Tafel slope typically suggests more efficient charge transfer and improved catalytic kinetics. As shown in Fig. 5c, the extracted Tafel slope values for 2H-MoS_2,1T-MoS_2, TM-1, TM-2, TM-5, TM-10, and Ti_3C_2 were 137, 81, 55, 70, 83, 91, and 203 mV dec^{-1}, respectively. Among these, TM-1 demonstrated the smallest Tafel slope (55 mV dec^{-1}), signifying its enhanced intrinsic catalytic performance relative to the other samples. This result also implies that the HER mechanism on TM-1 primarily follows the Volmer-Heyrovsky pathway[45]. TM-1 catalyst exhibits a Tafel slope of 55 mV dec^{-1}, which is superior to many previously reported systems, as shown in Table S2 and Fig. S7. The proposed mechanism of the 1T-MoS_2/Ti_3C_2 MXene is shown in the inset of Fig. 5b. In this pathway, a proton (H_3O^+) interacts with an electron (e^-) at the active catalytic site (*), producing an adsorbed hydrogen atom (H) through the step: $H_3O^+ + e^- + {}^* \rightarrow H^* + H_2O$. Subsequently, the H* species combines with another proton and electron to form molecular hydrogen (H_2), completing the reaction: $H_3O^+ + e^- + H^* \rightarrow H_2 + H_2O$.

The HER performance of an electrocatalyst is closely linked to its electrical conductivity, which affects charge transport efficiency. To investigate the interfacial charge transfer behavior and elucidate HER kinetics, electrochemical impedance spectroscopy (EIS) was conducted. This analytical method provides valuable insights into the electrode-electrolyte interface and characterizes the electrical response of catalytic systems. A key parameter for evaluating HER activity is the charge transfer resistance (R_{ct}). As illustrated in the Nyquist plots (Fig. 5d) and Table S3, among the samples tested, TM-1 demonstrated the lowest R_{ct} (91 Ω), indicating more efficient electron movement at the catalyst-electrolyte boundary. This resistance is notably lower than that of pristine 1T-MoS_2 (133 Ω), demonstrating that incorporating Ti_3C_2 MXene substantially enhances electron conductivity and overall HER performance[46]. This improvement is attributed to the strong interfacial interaction between Ti_3C_2 and MoS_2, which supports rapid charge transfer and reduces interfacial resistance. The solution resistance (R_s) of all catalysts falls within the range of 1–1.4 Ω, which is expected since all working electrodes were prepared using the same procedure and measured in the same electrolyte solution[17]. Furthermore, the Nyquist plots

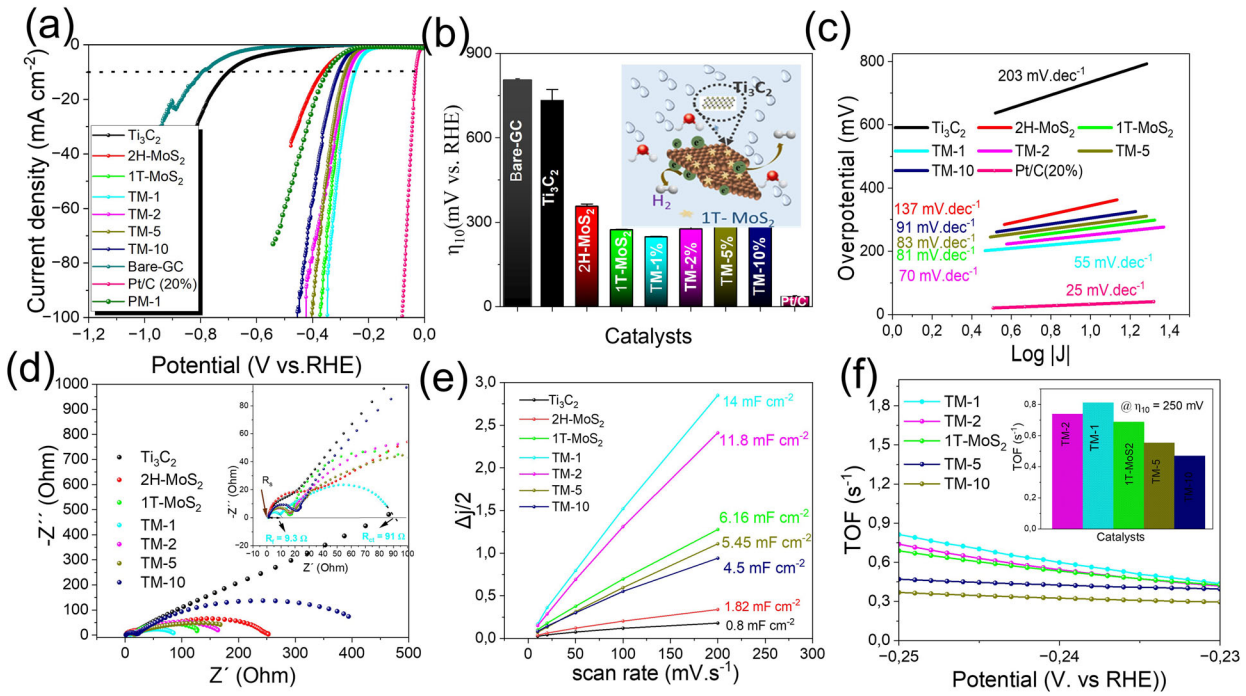


Fig. 5 | The electrochemical performance evaluation. Electrochemical measurements for hydrogen evolution in 0.5 M H_2SO_4: **a** LSV curves, **b** overpotential at j = 10 mA cm^{-2} for different electrocatalysts (inset: schematic representation of the mechanism involving TM-1, and Equivalent circuit used to stimulate the Nyquist plot), **c** corresponding Tafel plots, **d** EIS Nyquist plot of different catalysts (inset: enlarged high-frequency response of all composites), **e** capacitive Δj as a function of scan rate for different catalysts, and **f** TOF versus potential plot (inset: TOF values for composites at 250 mV).

for MoS_2-based catalysts reveal two distinct semicircular features: a smaller one at high frequencies related to surface texturing or porosity, and a larger semicircle at lower frequencies corresponding to the charge transfer process. The EIS spectra were fitted using the equivalent circuit shown in Fig. S5[9,47]. Fitted parameters are provided in Table S3.

The improved HER behavior of the composite is further supported by the synergistic combination of 1T-MoS_2 and Ti_3C_2, which enhances charge separation and lowers the energy barrier for hydrogen evolution[30]. Beyond charge transport, the availability of active catalytic sites plays a pivotal role in HER activity and is quantitatively represented by the electrochemically active surface area (ECSA). This metric, derived from non-Faradaic capacitive behavior, provides an independent assessment of active site density and intrinsic site activity[48]. To determine ECSA, cyclic voltammetry (CV) was performed at different scan rates in a potential window that excludes faradaic reactions (Fig. S4a–g). From these CV curves, the double-layer capacitance (C_{dl}) was extracted (Fig. 5e). As ECSA is directly proportional to C_{dl}[49], this value offers a proxy for comparing the accessible surface area across samples (Table S4). Ti_3C_2 MXene exhibited the lowest C_{dl} (0.8 mF cm^{-2}), likely due to nanosheet restacking that restricts active site exposure. Similarly, 2H-MoS_2 showed a modest C_{dl} (1.82 mF cm^{-2}), consistent with the low reactivity of its semiconducting basal planes. In contrast, 1T-MoS_2 and the composite materials demonstrated significantly enhanced C_{dl} values, underscoring the role of TMAOH-assisted phase conversion in increasing catalytic site density. Among all samples, TM-1 had the highest ECSA (350 cm^2), corresponding to a C_{dl} of 14 mF cm^{-2}. This is attributed to its enriched 1T-phase content (89%), which contributes both more active edge/basal sites and better conductivity. The significant increase in the number of active sites within the composites indicates that the presence of 1T-MoS_2, both on top of and within the interlayer spacing of Ti_3C_2 MXene, not only prevents aggregation but also enhances the accessibility of the aqueous electrolyte to the catalytically active surface. To assess the intrinsic activity of the catalysts, the polarization curves were normalized by the ECSA, as shown in Fig. S4h. After normalization, the result exhibited minimal differences, indicating that 1T-MoS_2 exhibits a bit higher intrinsic current density, indicating that most of the active sites originate from MoS_2. Increasing the Ti_3C_2 content reduces the effective MoS_2 active sites, leading to a decrease in intrinsic activity. It is important to note that while 1T-MoS_2 shows higher site-specific activity per unit surface area, TM-1 demonstrates the best overall catalytic performance due to the synergistic combination of high active site exposure and enhanced charge transfer (Ti_3C_2) across the 1T-MoS_2-Ti_3C_2 interface.

The turnover frequency (TOF) was further evaluated to quantify electron transfer efficiency and active site utilization from CV measurements[6,30]. TOF values were calculated in the potential range of 0.23 to 0.25 V versus RHE. As shown in Fig. 5f, TM-1 achieved the highest TOF at 0.81 s^{-1} at 250 mV overpotential, indicating superior site accessibility and electrocatalytic activity. This enhanced performance stems from the optimized 1T-MoS_2/Ti_3C_2 interface, which improves both surface exposure and charge transport, thereby elevating the overall HER efficiency.

To investigate the durability of the TM-1 electrocatalyst, cyclic voltammetry (CV) was conducted in 0.5 M H_2SO_4 at a scan rate of 100 mV s^{-1} (Fig. 6a). After 3000 consecutive cycles, the resulting polarization curves showed only slight deviation from the initial measurements, indicating the robust operational stability of TM-1. Stability over prolonged usage is a crucial metric for assessing electrocatalyst performance, especially in the context of industrial-scale hydrogen production. we employed chronopotentiometry to evaluate long-term electrochemical performance. TM-1 and a commercial 20 wt% Pt/C reference were tested under a steady current density of 10 mA cm^{-2}. The catalyst ink was uniformly deposited on one side of carbon paper, maintaining a mass loading of 0.32 mg cm^{-2}, and dried at 50 °C to ensure consistent testing conditions. As illustrated in Fig. 6b, TM-1 exhibited only a minor potential increase of 23 mV over 15 h, retaining more than 91% of its initial activity. The slight loss in stability (~9%) can be

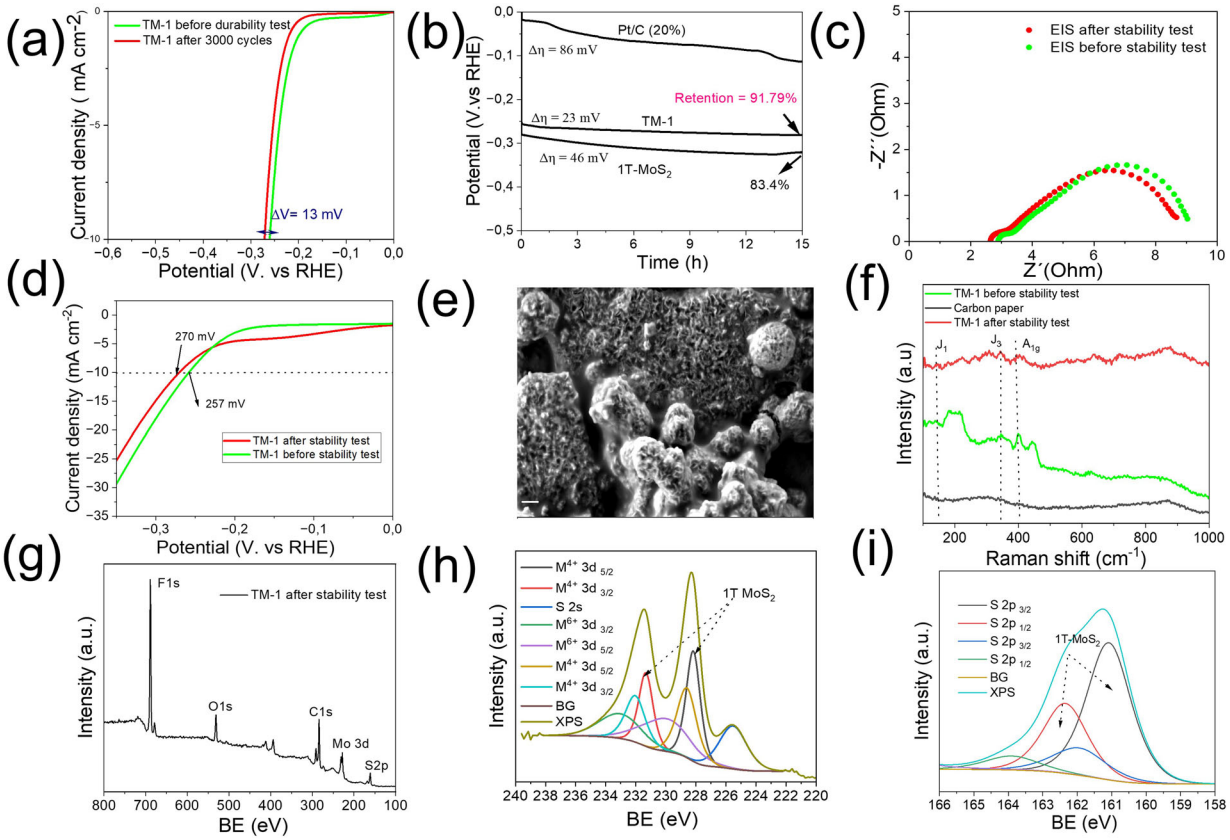


Fig. 6 | Stability evaluation and post-testing characterization of the TM-1 catalyst. a LSV polariztion curves of TM-1 before and after 3000 cycles, **b** Stability test of TM-1, 1T-MoS_2 and Pt/C (20%) under constant current density of 10 mA cm^{-2}, **c** EIS, **d** LSV, **e** SEM, **f** Raman of TM-1 before and after stability test, **g** XPS survey spectra of TM-1 after stability test, and Deconvoluted XPS spectra of **h** Mo 3d, and **i** S 2p for TM-1 after stability test.

attributed to partial 1T → 2H phase reversion, as the metastable 1T phase may gradually transform into the 2H phase during extended electrochemical operation, thereby reducing catalytic activity. Notably, this performance surpasses that of the Pt/C reference and highlights the remarkable stability of the nanocomposite during HER operation.

To further evaluate the contribution of Ti_3C_2 to catalytic durability, the stability of pristine 1T-MoS_2 was also examined under identical electrochemical conditions. As shown in Fig. 6b, 1T-MoS_2 retained 83.4% of its initial current density after 15 h of continuous HER operation, which is significantly lower than the retention observed for TM-1. This comparison confirms that the Ti_3C_2 support promotes structural stabilization of the 1T phase and facilitates more efficient charge transfer across the heterointerface, thereby improving long-term HER performance.

Post-stability tests were conducted at a current density of 10 mA cm^{-2} using EIS, LSV, SEM, Raman spectroscopy, and XPS to examine any structural or electrical degradation. EIS results revealed that the charge transfer resistance (R_{ct}) remained largely unchanged (Fig. 6c), indicating that electrical conductivity was preserved. Furthermore, the LSV curves recorded before and after the 15-h chronopotentiometry test were nearly superimposable (Fig. 6d), reinforcing the stability of the catalyst. SEM images of TM-1 after durability testing (Fig. 6e) confirmed that the nanosheet morphology was retained, with no signs of material degradation. Raman spectroscopy provided additional insight into the structural integrity of the 1T-MoS_2 phase following long-term testing. As shown in Fig. 6f, the post-test spectrum exhibited the distinctive vibrational modes of the 1T phase, including J_1 (~145 cm^{-1}), J_3 (~344 cm^{-1})[50], and A_{1g} (~402 cm^{-1}). Notably, the absence of the E^1_{2g} mode (~373 cm^{-1}), typically associated with the 2H phase, suggests that no significant phase transition from 1T to 2H occurred during electrolysis. The weaker visibility of the J_2 and J_3 modes in Fig. 1b compared to Fig. 6f arises from differences in measurement conditions and substrates. The as-synthesized catalysts in Fig. 1b were measured on glass under low laser power and short acquisition time, which can suppress weaker J-modes. In contrast, the post-stability sample on carbon paper (Fig. 6f) exhibits stronger J_2 and J_3 features due to substrate effects and structural relaxation after electrochemical processes testing.

Figure 6g–i presents the XPS spectra of the TM-1 catalyst after the HER stability test. The survey spectra confirm the continued presence of Mo, S, O, F, and C elements. The enhanced C signal is attributed to the underlying carbon paper substrate, while the F signal originates from the Nafion used as a bonding agent during sample preparation for the HER test. Notably, the Mo 3d and S 2p peaks characteristic of the 1T-MoS_2 structure remain well preserved after the HER test. However, the relative intensity analysis of the S 2p peak indicates a slight decrease in the 1T-phase content to 79.51%, suggesting that while some phase transformation may occur under prolonged electrochemical operation, a significant proportion of the catalytically active 1T phase remains intact. This highlights the structural robustness and catalytic relevance of the 1T-phase MoS_2 component during HER.

To further evaluate the catalyst under extended operational conditions, a 50 h chronoamperometric test was performed (Fig. S6a), where TM-1 maintained ~68% of its initial current density, demonstrating good long-term stability. To assess performance in industrially relevant environments, TM-1 was further tested at a high current density of 200 mA cm^{-2} for 24 h (Fig. S6b). SEM images taken after the stability tests (inset of Fig. S6b) show that the nanosheet morphology was preserved, with no evidence of material degradation. As shown in Fig. S6c, the catalyst exhibited minimal activity loss with only about a 72 mV decrease in LSV. Moreover, the Nyquist plots before and after stability (Fig. S6d) nearly overlap, indicating minimal change in R_{ct} and confirming robust charge-transfer kinetics. These observations demonstrate that TM-1 retains excellent stability and remains an efficient HER catalyst even under harsh operation.

Discussion

In this work, we report a scalable and one-step hydrothermal synthesis of a 2D/2D 1T-phase molybdenum disulfide (1T-MoS_2) and titanium carbide MXene (Ti_3C_2) heterostructure that demonstrates promising catalytic performance for the hydrogen evolution reaction (HER). Unlike prior studies, which often rely on multi-step procedures, inert atmospheres, or carbon coating to preserve MXene integrity, our approach uniquely incorporates tetramethylammonium hydroxide (TMAOH) to simultaneously induce the 1T phase in MoS_2 and stabilize Ti_3C_2 against oxidation during synthesis. Our key findings reveal that incorporating just 1 wt% Ti_3C_2 into the 1T-MoS_2 matrix forms a strong interfacial heterojunction, promoting fast charge transfer, a higher density of active sites, and improved phase stability. The optimized TM-1 composite achieved a low overpotential of 248 mV at 10 mA cm^{-2}, a Tafel slope of 55 mV dec^{-1}, and remarkable stability over 15 h. Compared to existing catalysts, our material achieves competitive and efficient HER kinetics with minimal synthesis complexity and material usage. This work paves the way for integrating this catalyst into full-cell electrolyzers and exploring its applicability in alkaline or neutral media, as well as expanding this method to other TMDs/MXene combinations for broader green hydrogen applications.

Methods

Synthesis of few-layer Ti_3C_2 MXene

Few-layer Ti_3C_2 MXene was synthesized by selectively removing the aluminum component from the Ti_3AlC_2 powder (≤40 µm, Carbon-Ukraine) using a hydrofluoric acid (HF, 48%, ACS reagent), based on a modified protocol from previous studies[33]. As HF is extremely hazardous and highly corrosive, all procedures were carried out in a well-ventilated fume hood with appropriate personal protective equipment, including acid-resistant gloves, face shield, and protective lab coat. Specifically, 1 g of Ti_3AlC_2 was added slowly to 20 mL of HF under ambient conditions and allowed to react for 24 h to ensure complete etching of the Al layers. After the reaction, the mixture was subjected to repeated centrifugation (five cycles at 3500 rpm for 5 min each) with deionized water until the pH of the supernatant reached around 6. To promote exfoliation, the washed sediment was redispersed in 15 mL of a 25% aqueous solution of tetramethylammonium hydroxide (TMAOH,9 99.9999%, ThermoFisher) and stirred for 24 h, facilitating the intercalation of TMA^+ ions between the MXene layers. The resulting dispersion, with a basic pH (~10), was washed twice (3500 rpm, 10 min each cycle) to neutralize the pH to about 7. After a final centrifugation step (1 h at 3500 rpm), the free-standing MXene film was collected by vacuum filtration using a Celgard membrane and then dried under vacuum at 70 °C overnight.

Preparation of 2H-MoS_2 Nanosheets

Ammonium heptamolybdate tetrahydrate ($(NH_4)_6Mo_7O_{24}.4H_2O$, CAS No.12054-85-2, 99.98%) and thiourea (CAS No. 62-56-6, ≥99%), both obtained from Sigma Aldrich, were used as received without further purification. For the synthesis, 0.617 g of ammonium heptamolybdate and 1.14 g of thiourea were dissolved in 20 mL of deionized water under vigorous stirring for 30 min to obtain a uniform solution. This precursor mixture was then sealed in a 45 mL Teflon-lined stainless-steel autoclave (filled to ~45% capacity) and subjected to hydrothermal treatment at 200 °C for 18 h. Once the autoclave cooled naturally to ambient temperature, the resulting black product was collected, thoroughly washed with both deionized water and ethanol using centrifugation at 8000 rpm for 10 min per wash cycle, and then dried under vacuum at 60 °C overnight.

Preparation of Ti_3C_2/1T-MoS_2 heterostructures

Hierarchical heterostructures composed of Ti_3C_2 and 1T-MoS_2 were fabricated via a hydrothermal synthesis approach, as schematically shown in Fig. 7. First, thiourea and ammonium heptamolybdate tetrahydrate were dissolved in 20 mL of deionized water. Subsequently, 0.3 g of tetramethylammonium hydroxide pentahydrate (TMAOH, $((CH_3)_4N(OH).5H_2O$, CAS No. 10424-65-4, Sigma Aldrich, ≥97%) was introduced to the solution. Varying amounts of Ti_3C_2 (corresponding to 1%, 2%, 5%, and 10% relative to the mass of $(NH_4)_6Mo_7O_{24}.4H_2O$) were incorporated to evaluate the effect on HER performance. These

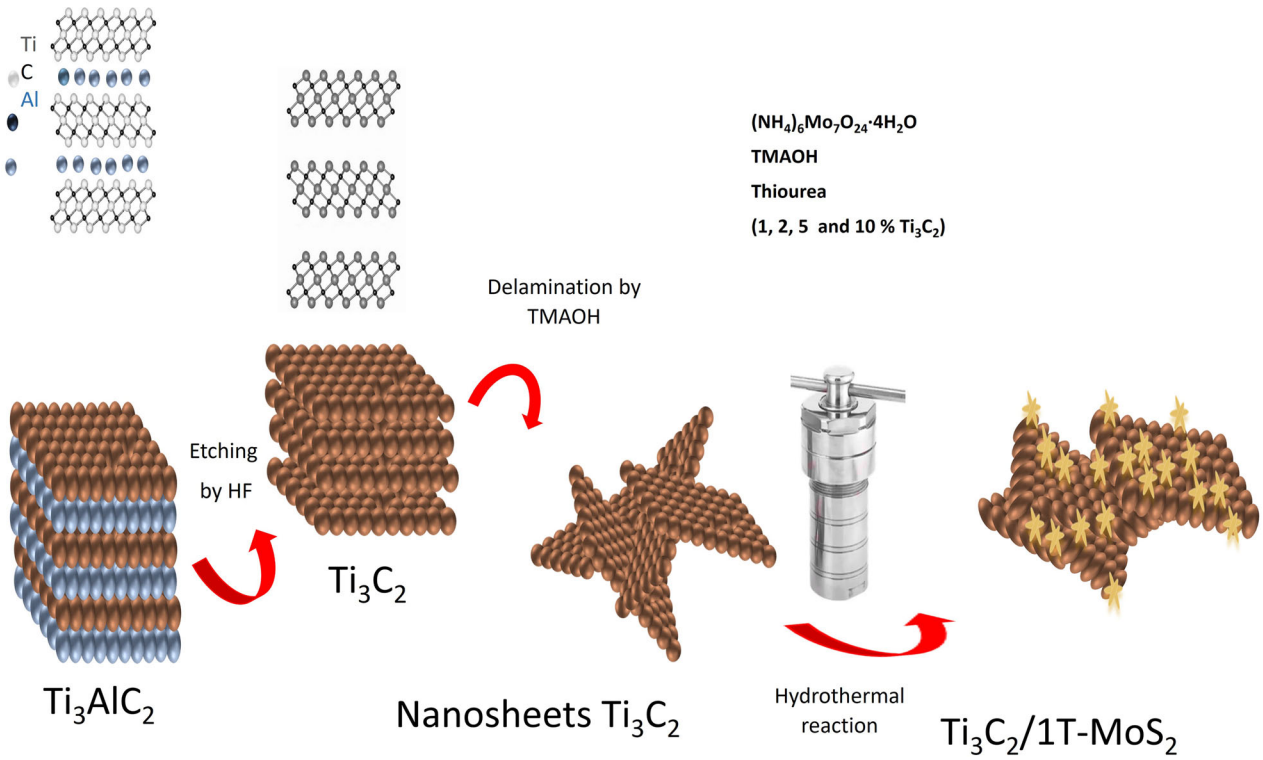


Fig. 7 | Schematics of experimentation. Schematically illustrates the preparation process of Ti_3C_2/1T-MoS_2 heterostructures.

resulting composites were designated as TM-1, TM-2, TM-5, and TM-10, respectively. The mixture was stirred vigorously for an additional 30 min to ensure homogeneity. The mixtures underwent hydrothermal treatment at 200 °C for 18 h, followed by washing and drying as above.

Preparation of 1T-MoS_2 nanosheets

As a reference sample, 1T-MoS_2 nanosheets were synthesized using the same procedure described for composites but without Ti_3C_2 addition. The process involved ammonium heptamolybdate (0.617 g), thiourea (1.14 g), and TMAOH (0.3 g).

Characterization

The crystalline phases and structural properties of the materials were characterized by X-ray diffraction (XRD) using a Bruker D8 ADVANCE diffractometer equipped with a copper Kα radiation source (λ = 1.5406 Å). Data were collected across a 2θ range of 5°–70°, with an increment of 0.02° per step. Raman spectroscopy was performed using an i-Raman Plus 532H portable spectrometer, operating with a 532 nm laser source. Thermogravimetric analyses (TGA) were performed on a NETZSCH TG 209F1 Iris instrument under a flow of Ar with a temperature range of 27–800 °C. Surface morphology was examined via scanning electron microscopy (SEM) on a ZEISS Gemini SEM 460 system, which features a field emission gun capable of operating in the 0.1–30 keV range.

Elemental composition and surface chemistry were analyzed by X-ray photoelectron spectroscopy (XPS) using a SPECS instrument fitted with a monochromatic Al K_α source (energy: 1486.7 eV) and a Phoibos 150 hemispherical analyzer. Survey scans were acquired with a pass energy of 100 eV, while core-level spectra were collected at 50 or 30 eV. The system operated under ultra-high vacuum conditions (≤10^{-9} mbar). An electron flood gun was employed to neutralize surface charging during measurement.

High-resolution structural and compositional imaging was conducted using a JEOL ARM200F transmission electron microscope (TEM) at 200 kV. This system was outfitted with CEOS aberration correctors for both probe and image formation, and a dual silicon drift detector for energy-dispersive X-ray spectroscopy (EDS). For high-angle annular dark field (HAADF) scanning transmission electron microscopy (STEM), a convergence semi-angle of ~27 mrad and a collection angle of 55 mrad were used. The STEM imaging resolution was around 0.8 Å, and EDS mapping provided elemental distributions at both nanometer and atomic resolutions.

Electrochemical measurements

Electrochemical measurements were performed at room temperature using a conventional three-electrode configuration connected to a CHI760E electrochemical workstation. A 0.5 M H_2SO_4 solution served as the electrolyte. The working electrode was a glassy carbon (GC) disk with a 2 mm diameter, while an Ag/AgCl electrode (saturated with KCl) and a carbon rod were used as the reference and counter electrodes, respectively. Catalyst ink for HER testing was prepared by dispersing 10 mg of the synthesized material in a solvent mixture containing 500 µL of deionized water, 500 µL of isopropanol, and 8 µL of 5 wt% Nafion solution (Sigma-Aldrich). The suspension was subjected to ultrasonic agitation for 30 min to ensure uniform dispersion. A 1 µL aliquot of the resulting ink was drop-cast onto the GC electrode, achieving an approximate catalyst loading of 0.32 mg cm^{-2}, and then air-dried under ambient conditions. For benchmarking, a commercial Pt/C (20 wt%) ink was prepared and deposited using the same protocol. Before testing, the electrolyte was deaerated by purging with nitrogen gas for 30 min. All measured potentials were calibrated against the reversible hydrogen electrode (RHE) using the equation: $E_{RHE} = E_{Ag/AgCl} + 0.059\,pH + 0.222$ V. Linear sweep voltammetry (LSV) was conducted at a scan rate of 5 mV s^{-1}, with 90% iR compensation. The double-layer capacitance (C_{dl}) was obtained by plotting half the difference in anodic and cathodic current densities (ΔJ/2) at 0.27 V vs. RHE against varying scan rates. The electrochemically active surface area (ECSA) was estimated using the relation: ECSA = C_{dl}/C_s, where C_s is the specific capacitance for standard electrode materials, with a literature value of 0.04 mF cm^{-2} used for carbon-based materials[6]. The turnover frequency (TOF) for each catalyst was determined by quantifying the number of active sites involved in the hydrogen evolution reaction. TOF, expressed in s^{-1}, was calculated using the equation: TOF (s^{-1}) = (J × S)/(2 × F × n)[18]. Where J represents the current density measured at various overpotentials, S (0.0314 cm^2) is the geometric

surface area of the electrode, and F (96500 C mol^{-1}) is the Faraday constant. The factor of 1/2 accounts for the number of electrons required to produce one hydrogen molecule, and n (in moles) is the number of active sites obtained using the cyclic voltammetry (CV) method, where $n = Q_s/F$. All CV tests were conducted in a solution of 0.5 M H_2SO_4 at a scan rate of 40 mV s^{-1}. The surface charge (Q_s) can be obtained by integrating the CV curve's charge over the whole potential range; the half value of the charge is the integrated charge over the entire potential range[18,51,52]. Electrochemical impedance spectroscopy (EIS) was performed across a frequency range of 0.1 Hz to 1 MHz, using a 5 mV AC amplitude and an applied overpotential of 250 mV vs. RHE. The catalyst durability was evaluated by conducting 3000 continuous CV cycles at a scan rate of 100 mV s^{-1}. Additionally, the chronopotentiometric stability of the catalyst was evaluated by applying a constant current density of 10 mA cm^{-2} for 15 h in 0.5 M H_2SO_4. The working electrode was prepared using an identical catalyst ink as described as previously described, ensuring consistent mass loading. The ink was drop-cast onto a 1 cm × 1 cm carbon paper substrate and allowed to dry under ambient conditions. Carbon paper was chosen due to its electrochemical inertness toward the HER, ensuring that observed activity originated solely from the catalyst.

Data availability

All data produced or analyzed in this study are included in this published article and its supplementary information files. No dedicated code was developed for this study.

Received: 29 September 2025; Accepted: 26 November 2025;
Published online: 15 December 2025

References

1. Akpasi, S. O. et al. Hydrogen as a clean energy carrier: advancements, challenges, and its role in a sustainable energy future. *Clean. Energy* **9**, 52–88 (2025).
2. Lontio Fomekong, R. et al. Ti_3AlC_2 MAX phase conversion to a novel 2D titanium carbo-oxide by an eco-friendly and low-cost method: highly selective gas sensing and supercapacitor evaluations. *J. Mater. Chem. C* **6045**, 6034 (2023).
3. McKone, J. R. et al. Evaluation of Pt, Ni, and Ni–Mo electrocatalysts for hydrogen evolution on crystalline Si electrodes. *Energy Environ. Sci.* **4**, 3573–3583 (2011).
4. Benson, J., Li, M., Wang, S., Wang, P. & Papakonstantinou, P. Electrocatalytic hydrogen evolution reaction on edges of a few layer molybdenum disulfide nanodots. *ACS Appl. Mater. Interfaces* **7**, 14113–14122 (2015).
5. Zargar, S. A. et al. Synthesis of novel 2D/2D Ti_3C_2Tx MXene / 1T-MoS_2 heterostructure enhanced with carbon nanotubes as a highly-efficient electrode for hybrid capacitive deionization. *J. Alloy. Compd.* **981**, 173765 (2024).
6. Wei, S. et al. Dual-phase MoS_2/MXene/CNT ternary nanohybrids for efficient electrocatalytic hydrogen evolution. *npj 2D Mater.* **6**, 25 (2022).
7. Boll, F. et al. In situ growth of layered 1T-MoS_2 onto carbon nanofibers as a strategy towards advanced hybrid materials for electrochemical energy storage and catalysis. *Nanoscale* **17**, 10706–10717 (2025).
8. Wang, M. et al. Two-dimensional layered heterojunctions for photoelectrocatalysis. *ACS Nano* **18**, 9245–9284 (2024).
9. Huang, L., Ai, L., Wang, M., Jiang, J. & Wang, S. Hierarchical MoS_2 nanosheets integrated Ti_3C_2 MXenes for electrocatalytic hydrogen evolution. *Int. J. Hydrog. Energy* **44**, 965–976 (2019).
10. Kong, W., Li, C. & Wu, W. A supercritical growth strategy for 1T/2H mixed-phase MoS_2 nanosheets of high activity and stability. *Int. J. Hydrog. Energy* **48**, 31582–31589 (2023).
11. Zhang, Y., Kuwahara, Y., Mori, K., Louis, C. & Yamashita, H. Hybrid phase 1T/2H-MoS_2 with controllable 1T concentration and its promoted hydrogen evolution reaction. *Nanoscale* **12**, 11908–11915 (2020).
12. Attanayake, N. H. et al. Effect of intercalated metals on the electrocatalytic activity of 1T-MoS_2 for the hydrogen evolution reaction. *ACS Energy Lett.* **3**, 7–13 (2018).
13. Venkateshwaran, S., Josline, M. J. & Senthil Kumar, S. M. Fine-tuning interlayer spacing in MoS_2 for enriching 1T phase via alkylated ammonium ions for electrocatalytic hydrogen evolution reaction. *Int. J. Hydrog. Energy* **46**, 8377–8390 (2021).
14. Jin, H. et al. Direct synthesis of 1T-phase MoS_2 nanosheets with abundant sulfur-vacancies through $(CH3)4N^+$ cation-intercalation for the hydrogen evolution reaction. *J. Mater. Chem. A* **9**, 13996–14003 (2021).
15. Gogotsi, Y. & Huang, Q. MXenes: two-dimensional building blocks for future materials and devices. *ACS Nano* **15**, 5775–5780 (2021).
16. Naguib, M. et al. Two-dimensional transition metal carbides. *ACS Nano* **6**, 1322–1331 (2012).
17. Akir, S. et al. Nanoengineering bismuth-modified vanadium carbide MXene for enhanced electrochemical performance in neutral electrolyte: a pathway toward high-performance supercapacitors. *J. Energy Storage* **85**, 110962 (2024).
18. Li, X. et al. Edge-oriented, high-percentage 1T'-phase MoS_2 nanosheets stabilize Ti_3C_2 MXene for efficient electrocatalytic hydrogen evolution. *Appl. Catal. B Environ.* **284**, 119708 (2021).
19. Bai, X. & Guan, J. MXenes for electrocatalysis applications: modification and hybridization. *Chin. J. Catal.* **43**, 2057–2090 (2022).
20. Li, J. et al. Nanosheets assembled layered MoS_2/MXene as high performance anode materials for potassium ion batteries. *J. Power Sources* **449**, 227481 (2020).
21. Wu X., Wang Z., Yu M., Xiu L. & Qiu J. Nanohybrids: stabilizing the MXenes by carbon nanoplating for developing hierarchical nanohybrids with efficient lithium storage and hydrogen evolution capability. *Adv. Mater.* **29**, 1607017 (2017).
22. Zheng, M. et al. MoS_2 intercalated p-Ti_3C_2 anode materials with sandwich-like three dimensional conductive networks for lithium-ion batteries. *J. Alloy. Compd.* **735**, 1262–1270 (2018).
23. Lim, K. R. G. et al. 2H-MoS_2 on Mo_2CT_x MXene nanohybrid for efficient and durable electrocatalytic hydrogen evolution. *ACS Nano* **14**, 16140–16155 (2020).
24. Attanayake, N. H. et al. Vertically aligned MoS_2 on Ti_3C_2 (MXene) as an improved HER catalyst. *J. Mater. Chem. A* **6**, 16882–16889 (2018).
25. Wu, Y. et al. MoS_2-nanosheet-decorated 2D titanium carbide (MXene) as high-performance anodes for sodium-ion batteries. *ChemElectroChem* **4**, 1560–1565 (2017).
26. Shuck, C. E. et al. Scalable synthesis of Ti_3C_2T MXene. *Adv. Eng. Mater.* **22**, 1901241 (2020).
27. Yu, P. et al. Binder-free 2D titanium carbide (MXene)/carbon nanotube composites for high-performance lithium-ion capacitors. *Nanoscale* **10**, 5906–5913 (2018).
28. Wang, L. et al. Tetrabutylammonium-intercalated 1T-MoS_2 nanosheets with expanded interlayer spacing vertically coupled on 2D delaminated MXene for high-performance lithium-ion capacitors. *Adv. Funct. Mater.* **31**, 2104286 (2021).
29. Wang, X. et al. 2D/2D 1T-MoS_2/Ti_3C_2 MXene heterostructure with excellent supercapacitor performance. *Adv. Funct. Mater.* **30**, 0190302 (2020).
30. Loh, J. Y., Yap, F. M. & Ong, W.-J. 2D/2D heterojunction interface: engineering of 1T/2H MoS_2 coupled with Ti_3C_2Tx heterostructured electrocatalysts for pH-universal hydrogen evolution. *J. Mater. Sci. Technol.* **179**, 86–97 (2024).
31. Xin, D. et al. Pre-intercalation of TMA cations in MoS_2 interlayers for fast and stable zinc ion storage. *Small* **20**, 2403050 (2024).
32. Rahmatinejad, J., Liu, X., Raisi, B. & Ye, Z. Synergistic cathode design for high-performance dual-salt magnesium/lithium-ion batteries using 2D/2D 1T/2H-MoS_2@Ti_3C_2T MXene nanocomposite. *Small* **20**, 2401391 (2024).

33. Alhabeb, M. et al. Guidelines for synthesis and processing of two-dimensional titanium carbide ($Ti_3C_2T_x$ MXene). *Chem. Mater.* **29**, 7633–7644 (2017).
34. Hu, T. et al. Vibrational properties of Ti_3C_2 and $Ti_3C_2T_2$ (T = O, F, OH) monosheets by first-principles calculations: a comparative study. *Phys. Chem. Chem. Phys.* **17**, 9997–10003 (2015).
35. Slot, T. K. et al. Surface oxidation of $Ti_3C_2T_x$ enhances the catalytic activity of supported platinum nanoparticles in ammonia borane hydrolysis. *2D Mater.* **8**, 015001 (2021).
36. Jia, X.-T. et al. Two-dimensional nanostructured $Ti_3C_2T_x$ MXene for ceramic materials: preparation and applications. *Nanomaterials* **15**, 204 (2025).
37. Ashok, A., Saseendran, S. B. & Asha, A. S. Synthesis of $Ti_3C_2T_x$ MXene from the Ti_3AlC_2 MAX phase with enhanced optical and morphological properties by using ammonia solution with the in-situ HF forming method. *Phys. Scr.* **97**, 025807 (2022).
38. Heng, C. et al. Ultrathin rare-earth-doped MoS_2 crystalline films prepared with magnetron sputtering and $Ar + H_2$ post-annealing. *Crystals* **13**, 308 (2023).
39. Li, Y. et al. 2D/2D/2D heterojunction of Ti_3C_2 MXene/MoS_2 nanosheets/TiO_2 nanosheets with exposed (001) facets toward enhanced photocatalytic hydrogen production activity. *Appl. Catal. B Environ.* **246**, 12–20 (2019).
40. Akir, S. et al. Atomic-layered V_2C MXene containing bismuth elements: 2D/0D and 2D/2D nanoarchitectonics for hydrogen evolution and nitrogen reduction reaction. *Nanoscale* **15**, 12648–12659 (2023).
41. Tian, R., Ding, Y., Wang, Q. & Song, P. Designing advanced 2D/2D heterojunctions of MoS_2 nanosheets/Ti_3C_2Tx MXene in gas-sensing applications. *Vacuum* **222**, 112991 (2024).
42. Remedios-Díaz, Y. et al. Highly active MoS_2-MXenes hybrid electrocatalysts towards the oxygen reduction reaction. *ChemElectroChem* **11**, e202300673 (2024).
43. Guo, T. et al. Hydrothermal synthesis of MXene-MoS_2 composites for highly efficient removal of pesticides. *Appl. Surf. Sci.* **588**, 152597 (2022).
44. Acerce, M., Voiry, D. & Chhowalla, M. Metallic 1T phase MoS_2 nanosheets as supercapacitor electrode materials. *Nat. Nanotechnol.* **10**, 313–318 (2015).
45. Wu, X., Wang, Z., Yu, M., Xiu, L. & Qiu, J. Stabilizing the MXenes by carbon nanoplating for developing hierarchical nanohybrids with efficient lithium storage and hydrogen evolution capability. *Adv. Mater.* **29**, 1607017 (2017).
46. Xue, Q. et al. Mn_3O_4 nanoparticles on layer-structured Ti_3C_2 MXene towards the oxygen reduction reaction and zinc–air batteries. *J. Mater. Chem. A* **5**, 20818–20823 (2017).
47. Yang, L. et al. Efficient hydrogen evolution catalyzed by amorphous molybdenum sulfide/N-doped active carbon hybrid on carbon fiber paper. *Int. J. Hydrog. Energy* **43**, 15135–15143 (2018).
48. Benck, J. D., Chen, Z., Kuritzky, L. Y., Forman, A. J. & Jaramillo, T. F. Amorphous molybdenum sulfide catalysts for electrochemical hydrogen production: insights into the origin of their catalytic activity. *ACS Catal.* **2**, 1916–1923 (2012).
49. Deng, S. J. et al. Phase modulation of (1T-2H)-$MoSe_2$/TiC-C shell/core arrays via nitrogen doping for highly efficient hydrogen evolution reaction. *Adv. Mater.* **30**, 1802223 (2018).
50. Gupta, U. et al. Characterization of few-layer 1T-$MoSe_2$ and its superior performance in the visible-light induced hydrogen evolution reaction. *APL Mater.* **2**, 092802 (2014).
51. Cheng, Y. et al. MoP_4/Ni_3S_2/MoO_3 heterogeneous structure nanorod arrays for efficient solar-enhanced overall water splitting. *J. Mater. Chem. A* **11**, 24764–24776 (2023).
52. Tian, P. et al. Ti_3C_2 nanosheets modified Zr-MOFs with Schottky junction for boosting photocatalytic HER performance. *Sol. Energy* **188**, 750–759 (2019).

Acknowledgements

This work was supported by an ERA Fellowship -Green Hydrogen of the German Academic Exchange Service (DAAD). We gratefully acknowledge the Helmholtz Association's Initiative and Networking Fund (Helmholtz Young Investigator Group VH-NG-1719) for the funding. M.P.B., P.W.M., and D.B. greatly acknowledge support from the German Federal Ministry of Education and Research in the framework of the project Catlab (03EW0015A/B). The authors would like to address particular thanks to R. Schwiddessen, M. Tovar, and K. Schwarzburg from the X-Ray and Microscopy and Spectroscopy Corelabs of the Helmholtz Zentrum Berlin for providing access to their facility and training on the equipment. Z.S. was supported by the Czech Science Foundation (GACR No. 23-05918S). Z.S. acknowledges the assistance provided by the Advanced Multiscale Materials for Key Enabling Technologies project, supported by the Ministry of Education, Youth, and Sports of the Czech Republic. Project No. CZ.02.01.01/00/22_008/0004558, Co-funded by the European Union and the project Advanced Functional Nanorobots (reg. No. CZ.02.1.01/0.0/0.0/15_003/0000444 financed by the EFRR) and ERC-CZ program (project LL2101) from the Ministry of Education, Youth and Sports (MEYS).

Author contributions

S.A. was responsible for the synthesis and characterization of the materials, as well as for writing the entire manuscript. B.S. performed the SEM measurement. D.B. aided in the synthesis of the initial materials. J.P. conducted and assessed the XPS results, as well as the TEM and EDS analyses. P.W.M. provided the precursors and laboratory facilities necessary to initiate the hydrothermal synthesis. Y.R.A. and Y.L. carried out the TGA measurements. Z.S. revised the manuscript. M.P.B. supervised the project, validated the results, and revised the manuscript. All authors reviewed the paper.

Competing interests

The authors declare no competing interests.

Additional information

Supplementary information The online version contains supplementary material available at https://doi.org/10.1038/s41699-025-00643-4.

Correspondence and requests for materials should be addressed to Sana Akir or Michelle P. Browne.

Reprints and permissions information is available at http://www.nature.com/reprints

Publisher's note Springer Nature remains neutral with regard to jurisdictional claims in published maps and institutional affiliations.

Open Access This article is licensed under a Creative Commons Attribution-NonCommercial-NoDerivatives 4.0 International License, which permits any non-commercial use, sharing, distribution and reproduction in any medium or format, as long as you give appropriate credit to the original author(s) and the source, provide a link to the Creative Commons licence, and indicate if you modified the licensed material. You do not have permission under this licence to share adapted material derived from this article or parts of it. The images or other third party material in this article are included in the article's Creative Commons licence, unless indicated otherwise in a credit line to the material. If material is not included in the article's Creative Commons licence and your intended use is not permitted by statutory regulation or exceeds the permitted use, you will need to obtain permission directly from the copyright holder. To view a copy of this licence, visit http://creativecommons.org/licenses/by-nc-nd/4.0/.

© The Author(s) 2025